CHAPTER 3

PARABOLIC TAPERING WIDTH PVEH UNDER TRANSVERSE EXCITATION

This chapter presents an experimentally validated full nonlinear model of a novel parabolic tapering width base excited PVEH. The electromechanically coupled motion equations are formulated using Hamilton's equation and Gauss' theorem. The geometric and material nonlinearities are considered in the form of nonlinear piezoelectric constitutive relation, electric displacement relation, and strain-displacement relation. Galerkin's discretization approach is used to discretize the energy expressions. The MMS and chain rule with detuning parameter is used to obtain the system's responses. Finally, the effects of the taper parameter and PZT thickness on the system's performance and nonlinearity are investigated and discussed.

3.1 Outline

A PVEH is typically a cantilever structure with piezoelectric patches bonded to the surface. Which is attached to a vibrating system, and the free end usually carries tip load mass. Traditionally, rectangular cantilever beams are used in PVEHs. However,

researchers have investigated a range of techniques to boost the performance of PVEHs, including innovative geometry-modified/tapered cantilever structures. A complex electrical circuit comprising AC~DC conversion is connected in real-world applications to enable power processing and storage. However, to formulate mathematical models for the PVEH, researchers often consider the open-circuit (OC) voltage response or occasionally a simple resistive load. The mathematical modeling used in energy harvesting literature includes lumped parameter models, distributed parameter models, geometrically and materially nonlinear models, and approximate solution approaches. In a distributed parameter model, the structure's inertia and elasticity are supposed to be continuously distributed. Although the lumped parameter technique provides a basic knowledge of a PVEH system, it is oversimplified and leaves out several key elements. Furthermore, the nonlinear models and approximate solution approaches are essential for correctly estimating the harvester's responses at higher excitation levels.

3.2 Nonlinear Mathematical Modeling

The electromechanically coupled motion equations of the proposed base excited parabolic tapering width PVEH with a tip load are formulated using Hamilton's equation and Gauss' theorem. The line diagram of the proposed parabolic tapering width beam is shown in Figure 3.1. The width of the host structure and the PZT patch, are varying following the relation $b(x)=b_0\left(1-4\sqrt{\phi x}\right)$. In this context $\phi=\left(a/b_0^2\right)$ is the taper parameter. The width variation relation is derived from the Figure 3.1 as follows;

$$\frac{b(x)}{2}=\frac{b_0}{2}-y(x)$$

$$\Rightarrow b(x) = b_0 - 2\sqrt{4ax} \qquad \left(\because y = \sqrt{4ax}\right)$$
$$= b_0 - 4\sqrt{ax} = b_0\left[1 - 4\sqrt{\left(\frac{a}{b_0^2}\right)x}\right] \tag{3.1}$$
$$= b_0 - 4\sqrt{\phi x}$$

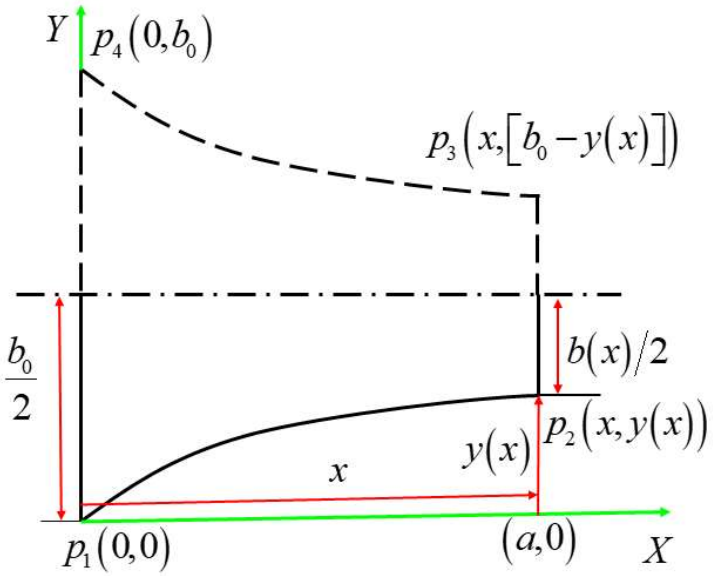

Figure 3.1 Line diagram of the parabolic tapering width harvester

3.2.1 Theoretical framework

The proposed composite piezoelectric-coupled parabolic tapering width PVEH with a harvesting beam consist of a PZT patch attached over the central host beam is shown in Figure 3.2. The harvester has one end tied with a weight block to bring down the harvester's resonant frequency for low-frequency applications. The other end is fixed at the *Y*-axis, where the base excitation is applied as portrayed in Figures. 3.2a and 3.2b. The cross-sectional area of the host structure and the PZT patch are varying following

the relation $A_p(x)=b(x)t_p$ and $A_h(x)=b(x)t_h$. Figure 3.2c shows the PZT-coupled beam cross-section with the neutral axis position, where $E_hI_h(x)=\frac{E_h(z_1^3-z_0^3)}{3}b(x)$ and $E_pI_p(x)=\frac{E_p(z_2^3-z_1^3)}{3}b(x)$ are the flexural rigidity of the host beam and the PZT-patch, respectively, at any standard section. The position of Z_0, Z_1, and Z_2 are also shown in Figure 3.2c.

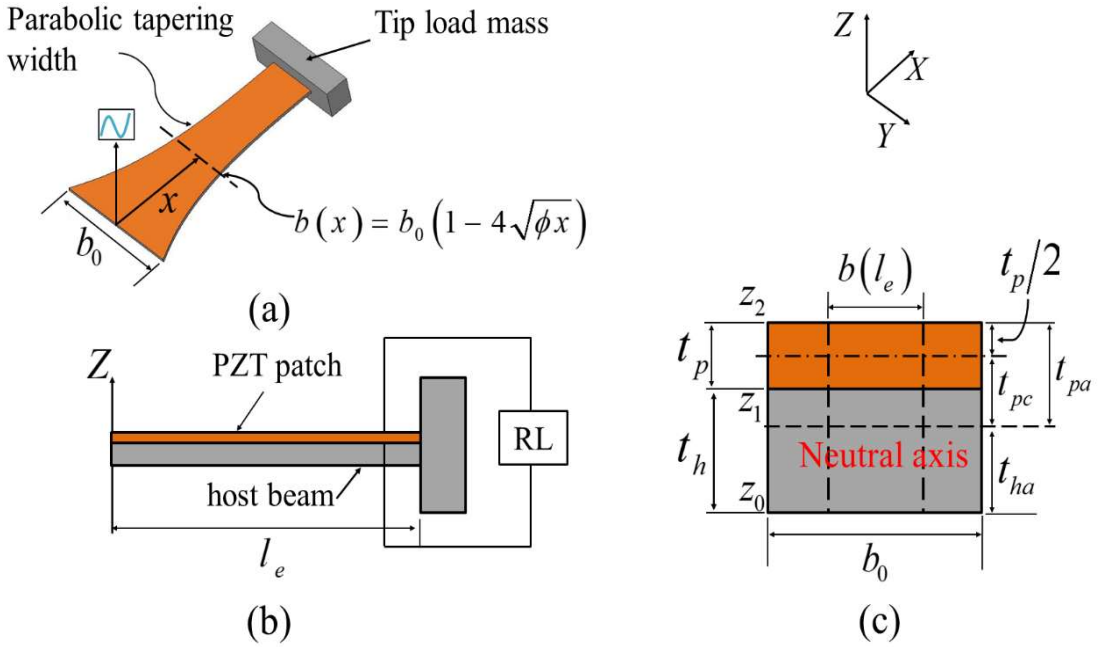

Figure 3.2 Schematics of the parabolic converging width PZT-coupled VEH with tip mass. The fixed end is at Y-axis and parallel to the Earth's surface (a) Isometric view, (b) front view, and (c) PZT-coupled beam cross-section

3.2.2 Nonlinear electromechanical equations

The extended Hamilton's principle(Meirovitch, 2001) and the Gauss theory is applied to formulate the nonlinear coupled electromechanical motion equations as;

$$\frac{d}{dt}\frac{\partial l}{\partial \dot{q}}-\frac{\partial l}{\partial q}=\frac{\delta W^{e}}{\delta q_{i}},\quad i=1,2,\cdots,n \tag{3.2}$$

$$\frac{d}{dt}\int_{A} D_{3}dA=\frac{v(t)}{R_{L}} \tag{3.3}$$

Here, the virtual work done is due to the damping and external excitation applied. The Lagrangian is calculated utilizing the total kinetic energy and potential energy as:

$$l=T^{e}-U^{e} \tag{3.4}$$

The total kinetic energy of the PVEH system; a combination of the PZT-coupled structure and the tip load mass' kinetic energies considering $u_x(x,t),u_y(x,t),u_z(x,t)$ as the displacements along (*x, y, z*) direction, is expressed as;

$$K^{e}=\int_{0}^{l_e}\left\{\rho_h A_h(x)+\rho_p A_p(x)\right\}\left(\dot{u}_x{}^2+\dot{u}_z{}^2\right)dx+\frac{1}{2}M_{LM}\left(\dot{u}_x{}^2+\dot{u}_z{}^2\right)_{x=l_e}+\frac{1}{2}I_{LM}\left(\dot{u}_z'^2\right)_{x=l_e} \tag{3.5}$$

For small extensional deflections, the relationships between the extensional and transverse deflections are calculated as:

$$u_x=-\frac{1}{2}\int_{0}^{h}u_z'^2dh \tag{3.6}$$

Substituting Equation (3.6) into Equation (3.5) and implementing the parabolic tapering width relation gives;

$$\begin{aligned}K^{e}=&\left(\rho_h A_h+\rho_p A_p\right)\left(\int_{0}^{l_e}\left(\dot{u}_z{}^2\right)\left(1-4\sqrt{\phi x}\right)dx+\int_{0}^{l_e}\left(\int_{0}^{x}u_z'\dot{u}_z'dh\right)\left(\int_{0}^{x}u_z'\dot{u}_z'dh\right)\left(1-4\sqrt{\phi x}\right)dx\right)\\&+\frac{1}{2}M_{LM}\left[\left(\int_{0}^{l_e}u_z'\dot{u}_z'dx\right)\left(\int_{0}^{l_e}u_z'\dot{u}_z'dx\right)+\left(\dot{u}_z{}^2\right)_{x=l_e}\right]+\frac{1}{2}I_{LM}\left(\dot{u}_z'^2\right)_{x=l_e}\end{aligned} \tag{3.7}$$

The total potential energy of the PVEH is expressed using the stress-strain relation as follows:

$$U^e = \frac{1}{2}\int_0^{l_e}\int_A T_1^h S_1 dA dx + \frac{1}{2}\int_0^{l_e}\int_A T_1^p S_1 dA dx \tag{3.8}$$

The nonlinear unidirectional displacement-strain relation for the system, neglecting the extensional strain (along *x*-direction) and considering the transverse displacement (along the *z*-direction) to be small and equal for every point on a cross-section, can be written as(Nayfeh and Pai, 2004):

$$S_1 = -z\left(u_z'' + \frac{1}{2}u_z'' u_z'^2\right) \tag{3.9}$$

At high excitation amplitude, the geometrical nonlinearity appears, and the piezoelectric material acts nonlinearly. Hence, the nonlinear constituent relations for the PZT-patches are considered(Arafa and Baz, 2004) as;

$$T_1^p = E_p S_1 - e_{31}E_3 + \frac{1}{2}c_1 S_1^{\,2} + \frac{1}{2}c_2 E_3^{\,2} - c_3 E_3 S_1 \tag{3.10}$$

and for the isotropic host beam material, the constitutive relation is expressed as;

$$T_1^h = E_h S_1 \tag{3.11}$$

The nonlinear electric displacement relation is considered as;

$$D_3 = e_{31}S_1 + \varepsilon_{33}^s E_3 + \frac{1}{2}c_3 S_1^2 + \frac{1}{2}c_4 E_3^2 - c_2 E_3 S_1 \tag{3.12}$$

In Equations (3.10) and (3.12), c_1, c_2, c_3, and c_4 are the nonlinear piezoelectric coefficients. The voltage across the PZT patch can be related to the electric field along z-direction E_3 as;

$$v(t) = -E_3 t_p \tag{3.13}$$

To expand the total potential energy expression of the parabolic tapering width PVEH, Equations (3.9) – (3.13) are substituted into Equation (3.8) as;

$$U^e = \frac{1}{2}\left\{\begin{array}{l}\left(E_h I_h + E_p I_p\right)\left(\int_0^{l_e}\left(u_z''^2 + u_z''^2 u_z'^2\right)\left(1-4\sqrt{\phi x}\right)dx\right) - e_{31}\dfrac{v(t)b_0}{t_p}\left(z_2^2 - z_1^2\right) \\ \times\left(\int_0^{l_e}\left(u_z'' + \dfrac{1}{2}u_z'' u_z'^2\right)\left(1-4\sqrt{\phi x}\right)dx\right) - \dfrac{c_1}{8}b_0\left(z_2^4 - z_1^4\right)\left(\int_0^{l_e} u_z''^3\left(1-4\sqrt{\phi x}\right)dx\right) \\ -\dfrac{1}{4}\dfrac{c_2\left(z_2^2 - z_1^2\right)}{t_p^{\,2}}b_0\left(\int_0^{l_e}\left(u_z'' + \dfrac{1}{2}u_z'' u_z'^2\right)\left(1-4\sqrt{\phi x}\right)dx v^2(t)\right) \\ +\dfrac{c_3}{3t_p}b_0\left(z_2^3 - z_1^3\right)\left(\int_0^{l_e}\left(u_z''^2 + u_z''^2 u_z'^2\right)\left(1-4\sqrt{\phi x}\right)dx v(t)\right)\end{array}\right\} \tag{3.14}$$

The virtual work done due to exciting acceleration on the beam and the tip mass, and due to the structural damping is given as;

$$\begin{aligned}\delta W^e = &-\int_0^{l_e}\left(A_h\rho_h + A_p\rho_p\right) f\cos(\varpi t)\left(1-4\sqrt{\phi x}\right)\delta u_z dx - M_{LM} f\cos(\varpi t)\left(\delta u_z\right)_{x=l_e} \\ &-\int_0^{l_e} C_a\dot{u}_z + \frac{\partial^2}{\partial x^2}\left(\left(I_h(x) + I_h(x)\right)C_s\frac{\partial^3 u_z}{\partial t\partial x^2}\right)\delta u_z dx\end{aligned} \tag{3.15}$$

3.2.3 Galerkin's discretization

The frequency characteristics and the motion equations for the PZT-coupled system are obtained based on Hamilton's equation. Before that, Galerkin's discretization technique

is applied to discretize the total kinetic and potential energies and the virtual work done. For which, the transverse displacement component $u_z(x,t)$ is assumed as a combined expansion of spatial function multiplied by temporal coordinates and expressed as;

$$u_z(x,t)=\sum_{i=1}^{n}\psi_i(x)s_i(t) \tag{3.16}$$

in which, $\psi_i(x)$ for the cantilever beam is adopted from Parida and Dash(2016).

The first governing motion equation for the parabolic tapered PVEH, including geometry and material nonlinearities, is obtained by substituting Equation (3.16) into Equations (3.7), (3.14), and (3.15) and finally replacing in Equation (3.2) as;

$$\begin{aligned}&\sum_{j=1}^{n}M_{ij}\ddot{s}_j+2\zeta_i\omega_i\dot{s}_i-\sum_{j=1}^{n}\sum_{k=1}^{n}B_{ijk}s_js_k-\sum_{j=1}^{n}\sum_{k=1}^{n}D_{ijk}s_js_kv(t)\\&+\sum_{j=1}^{n}\sum_{k=1}^{n}\sum_{l=1}^{n}f_{ijkl}\left(s_j\dot{s}_k\dot{s}_l+s_js_k\ddot{s}_l\right)+\sum_{j=1}^{n}F_{ij}s_jv(t)+\sum_{j=1}^{n}H_{ij}s_j-\gamma_iv(t)\\&+\sum_{j=1}^{n}\sum_{k=1}^{n}\sum_{l=1}^{n}Y_{ijkl}s_js_ks_l-\lambda_iv^2(t)=\Delta_if\cos(\varpi t)\end{aligned} \tag{3.17}$$

The coefficients of the Equation (3.17) are given in Appendix I. The second governing equation is obtained by substituting Equation (3.12) into Equation (3.3) as;

$$\begin{aligned}&-e_{31}b_0t_{pc}\int_0^{l_e}\left(\dot{u}_z''+\frac{1}{2}\dot{u}_z''u_z'^2+u_z''u_z'\dot{u}_z'\right)\left(1-4\sqrt{\phi x}\right)dx-\frac{\varepsilon_{33}^{s}b_0}{t_p}\int_0^{l_e}\left(1-4\sqrt{\phi x}\right)dx\dot{v}(t)\\&+c_3t_{pc}^2b_0\int_0^{l_e}u_z''\dot{u}_z''\left(1-4\sqrt{\phi x}\right)dx+\frac{c_4b_0}{t_p^2}\int_0^{l_e}\left(1-4\sqrt{\phi x}\right)dxv(t)\dot{v}(t)\\&-\frac{c_2t_{pc}b_0}{t_p}\int_0^{l_e}\left(u_z''+\frac{1}{2}u_z''u_z'^2\right)\left(1-4\sqrt{\phi x}\right)dx\dot{v}(t)\\&-\frac{c_2t_{pc}b_0}{t_p}\int_0^{l_e}\left(\dot{u}_z''+\frac{1}{2}\dot{u}_z''u_z'^2+u_z''u_z'\dot{u}_z'\right)\left(1-4\sqrt{\phi x}\right)dxv(t)=\frac{v(t)}{R_L}\end{aligned} \tag{3.18}$$

Discretizing Equation (3.18) gives;

$$\sum_{i=1}^{n}\varphi_i\dot{s}_i+\sum_{i=1}^{n}\sum_{j=1}^{n}\sum_{k=1}^{n}L_{ijk}s_is_j\dot{s}_k+C\dot{v}(t)-\sum_{i=1}^{n}\sum_{j=1}^{n}G_{ij}s_i\dot{s}_j-c_{4v}v(t)\dot{v}(t)$$
$$+\sum_{i=1}^{n}k_is_i\dot{v}(t)+\sum_{i=1}^{n}\chi_i\dot{s}_iv(t)+\frac{v(t)}{R_L}=0 \tag{3.19}$$

The coefficients of the Equation (3.19) are given in Appendix I.

3.2.4 Response analysis

The vibration energy harvesters are designed to operate at first natural frequencies. Therefore, the first principal mode shape is considered to formulate the governing motion equations as,

$$\ddot{s}_1+2\zeta_1\omega_1\dot{s}_1+\omega_1^2s_1-\gamma_1v(t)-B_{111}s_1^2+Y_{1111}s_1^3-\lambda_1v^2(t)+f_{1111}\left(s_1\dot{s}_1^2+s_1^2\ddot{s}_1\right)$$
$$-D_{111}s_1^2v(t)+F_{11}s_1v(t)=\Delta_1 f\cos(\varpi t) \tag{3.20}$$

$$\varphi_1\dot{s}_1+L_{111}s_1^2\dot{s}_1+C\dot{v}(t)-G_{11}s_1\dot{s}_1-c_{4v}v(t)\dot{v}(t)+k_1s_1\dot{v}(t)+\chi_1\dot{s}_1v(t)+\frac{v(t)}{R_L}=0 \tag{3.21}$$

The orthogonality conditions for the parabolic tapered beam, implemented in Equation (3.20), are(Salmani et al., 2015);

$$\left(\rho_hA_h+\rho_pA_p\right)\int_0^{l_e}\psi_i\psi_j\left(1-4\sqrt{\phi x}\right)dx+M_{LM}\psi_i(l_e)\psi_j(l_e)+I_{LM}\psi_i'(l_e)\psi_j'(l_e)=\delta_{ij}$$
$$\left(E_hI_h+E_pI_p\right)\int_0^{l_e}\psi_i''\psi_j''\left(1-4\sqrt{\phi x}\right)dx=\omega_i^2 \tag{3.22}$$

The method of multiple scales (MMS), which has been widely employed by researchers to solve nonlinear PVEH problems(Abdelkefi et al., 2012a, 2012b; Daqaq et al., 2009; Garg and Dwivedy, 2016; Masana and Daqaq, 2011), is implemented to obtain the

solutions of the coupled nonlinear Equations (3.20) and (3.21) by considering the time-dependent as;

$$T_n = \xi^n t \tag{3.23}$$

The implementation of chain rule gives the derivatives of time as,

$$\frac{d}{dt} = C_0 + \xi C_1 + \xi^2 C_2 + o\left(\xi^3\right) \text{ and } \frac{d^2}{dt^2} = C_0^2 + 2\xi C_0 C_1 + \xi^2 C_1 + 2\xi^2 C_0 C_2 + o\left(\xi^3\right) \tag{3.24}$$

where $C_n = \partial / \partial T_n$. Therefore, the solutions of the system are expanded as

$$s_1(t) = s_{10}\left(T_0, T_1, T_2\right) + \xi s_{11}\left(T_0, T_1, T_2\right) + \xi^2 s_{12}\left(T_0, T_1, T_2\right) + o\left(\xi^3\right) \tag{3.25}$$

$$v(t) = v_0\left(T_0, T_1, T_2\right) + \xi v_1\left(T_0, T_1, T_2\right) + \xi^2 v_2\left(T_0, T_1, T_2\right) + o\left(\xi^3\right) \tag{3.26}$$

Since the nonlinear coupling terms are of smaller orders of magnitude compared to their linear counterparts(Masana and Daqaq, 2011), the scaled coefficients are given as;

$$\begin{cases} \xi^0 \omega_1, \xi^0 \varphi_1, \xi^0 C, \xi^0 1/R_L \\ \xi^1 B_{111}, \xi^1 \lambda_1, \xi^1 F_{11}, \xi^1 L_{111}, \xi^1 G_{11}, \xi^1 c_{4v}, \xi^1 k_1, \xi^1 \chi_1 \\ \xi^2 \zeta_1, \xi^2 \gamma_1, \xi^2 Y_{1111}, \xi^2 f_{1111}, \xi^2 D_{111}, \xi^2 \Delta_1 \end{cases} \tag{3.27}$$

Furthermore, to approach the excitation frequency to the first natural frequency, a detuning parameter σ is introduced as(Garg and Dwivedy, 2016);

$$\varpi = \omega_1 + \xi^2 \sigma \tag{3.28}$$

The Equations (3.24) – (3.28) are substituted into Equations (3.20) and (3.21), and six differential equations are obtained by equating the same powers of ξ to zero as given in Appendix I.

The solution of Equation (I.1) is assumed as;

$$s_{10}\left(T_0,T_1,T_2\right)=A_{11}\left(T_1,T_2\right)e^{i\omega_1 T_0}+\bar{A}_{11}\left(T_1,T_2\right)e^{-i\omega_1 T_0} \tag{3.29}$$

Applying Equation (3.29), the solution of Equation (I.2) can be stated as;

$$v_0\left(T_0,T_1,T_2\right)=\frac{i\varphi_1\omega_1 A_{11}\left(T_1,T_2\right)R_L e^{i\omega_1 T_0}}{iCR_L\omega_1+1}-\frac{i\varphi_1\omega_1\bar{A}_{11}\left(T_1,T_2\right)R_L}{\left(iCR_L\omega_1-1\right)e^{i\omega_1 T_0}} \tag{3.30}$$

Substitution of Equations (3.29) and (3.30) in Equation (I.3) and equating the secular terms to zero gives $B_1 A_{11}\left(T_1,T_2\right)=0$, which implies that A_{11} is a function of T_2. The solution of $A_{11}\left(T_2\right)$ is accomplished by equating the secular terms of Equation (I.5) to zero, after substituting the solutions of Equations (I.1) to (I.4). For that, the following polar form of A_{11} is used as;

$$A_{11}\left(T_2\right)=\frac{1}{2}a\left(T_2\right)e^{i\tau\left(T_2\right)},\quad \bar{A}_{11}\left(T_2\right)=\frac{1}{2}a\left(T_2\right)e^{-i\tau\left(T_2\right)} \tag{3.31}$$

The steady-state solution is obtained by substituting Equation (3.31) into the secular terms equation, and implementing the transformation $\sigma T_2-\tau\left(T_2\right)=\theta$, in addition to vanishing $d/dT_2\, a\left(T_2\right)$ and $d/dT_2\,\theta\left(T_2\right)$. The real and imaginary fragments of the secular terms are individually equated to zero as:

$$\begin{cases}\Re:\dfrac{1}{2}f\Delta_1\cos\left(\theta\right)+o_1 a\left(T_2\right)+o_2 a^2\left(T_2\right)+o_3 a^3\left(T_2\right)=0\\ \Im:\dfrac{1}{2}f\Delta_1\sin\left(\theta\right)+k_1 a\left(T_2\right)+k_2 a^2\left(T_2\right)+k_3 a^3\left(T_2\right)=0\end{cases} \tag{3.32}$$

The coefficients of Equation (3.32) are given in Appendix II.

The value of $a(T_2)$ in Equation (3.31) in relation to σ is expressed as;

$$\frac{1}{4}f^2\Delta_1^2 = \left(k_1 a(T_2) + k_2 a^2(T_2) + k_3 a^3(T_2)\right)^2 + \left(o_1 a(T_2) + o_2 a^2(T_2) + o_3 a^3(T_2)\right)^2 \quad (3.33)$$

Therefore, adopting the parameter $a(T_2)$, the magnitude of the voltage generated from the harvester can be calculated as;

$$|v_0| = \frac{\omega_1 \varphi_1 R_L}{\sqrt{(R_L \omega_1 C)^2 + 1}} a(T_2) \quad (3.34)$$

3.3 Mathematical Model Validation

Prior to estimating the PVEH's performance and investigate the effects of taper and PZT patch thickness on the nonlinearity, the proposed mathematical model is validated through earlier reported numerical models and experimental methods.

3.3.1 Validation through earlier models

The present nonlinear formulation is compared with the nonlinear mathematical models presented by Abdelkefi et al.(2012a) and Salmani and Rahimi(2018). The comparison is made by estimating the current PVEH's output voltage using the three nonlinear formulations. Table 3.1 compares the output voltage obtained from the VEH using the present formulation and the two earlier presented formulations for the base excitation amplitudes of 1g, 4g, 7g, and 10g. It can be seen that the current results are in decent

agreement with those of the other two. Hence, the proposed numerical formulations are well suited for calculating the performance of the parabolic tapering width PVEH.

Table 3.1 Comparison of the output voltage from the VEH using different nonlinear formulations for 1g, 4g, 7g, and 10g base excitation amplitudes

	Output voltage (Volt)			
	V(1g)	V(4g)	V(7g)	V(10g)
Present formulation	1.6715	3.5337	6.1781	7.8443
Abdelkefi et al.(2012a)	1.6126	3.5268	6.1583	7.8266
Salmani and Rahimi(2018)	1.6435	3.5287	6.1619	7.8325

3.3.2 Validation through experimental method

In order to validate the proposed formulations, an experiment is set up using a parabolic tapered PVEH. For this purpose, a system with $\phi = 0.4$, $M_{LM} = 15.1808$ gram, and the dimensions given in Table 3.2 are considered. The physical properties of PZT-5H are listed in Table 1.1. The details of prototype fabrication, setup construction, experimental method, and typical signals from the digital storage oscilloscope (DSO) are given in Appendix III.

Table 3.2 Physical properties of the PVEH's components

Dimensions/properties	PZT-5H	Brass
E (GPa), ρ(kg/m^3)	-	97, 8490
Thickness (mm)	0.254	0.5
Length (mm)	72	72
Base width (mm)	50	50

In order to validate the proposed numerical model using the experiment, the damping ratio must be measured. For this purpose, an investigation is carried out with the harvester under a small excitation amplitude. The principal natural frequency and damping ratio calculated from the experiment are 16.62 Hz and 2.9 %, respectively. After that, the experiments were conducted for the acceleration levels 1 g, 4 g, 7 g, and 10g in a frequency band of 10 Hz- 25Hz. The numerical solution is likewise carried out using the identical parameters and acceleration amplitudes as those used in the experiments. Using the least square method and the experimental results, the nonlinear piezoelectric coefficients c_i; i = 1…4, are identified. The identified values are $c_1 = -5.8\times10^{13}$ Pa, $c_2 = 6.1\times10^{-5}$ N/V^2, $c_3 = -6.7\times10^{5}$ C/m^2, and $c_4 = 2.2\times10^{-10}$ C/V^2. Since the electric field's magnitude is small in the case of vibration energy harvesting, the coefficients c_2 and c_4 can be neglected. The responses of the model are obtained considering and ignoring c_2 and c_4 shown in Figure 3.3. The identical voltage curves for both the cases concluded that the higher-order coefficients c_2 and c_4 can be overlooked for the proposed PVEH system. The numerical results of the coefficients of Equations (3.17) and (3.19) are presented in Table 3.3.

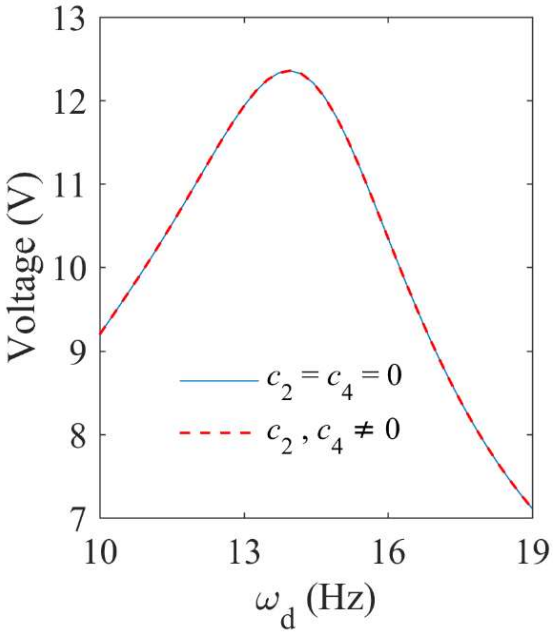

Figure 3.3 Output voltage for 10 g excitation amplitude with $t_p = 0.254$ mm, $l_e = 80$ mm, $\phi = 0.4$, $b_0 = 50$ mm, $t_h = 0.5$ mm, $M_{LM} = 15.1808$ gram considering and neglecting c_2 and c_4

Table 3.3 Numerical values of the coefficients

Coefficient	Value	Coefficient	Value
M_{11}(kg)	0.031	α_1(C)	-2.221×10^{-4}
H_{11}(N/m)	1.8×10^{5}	α_2(Nm^3)	-0.088
γ_1(N/V)	-0.126	α_3(Nm/V^2)	1.027×10^{-6}
B$_{111}$(N/m^2)	-1.081×10^{8}	α_4(cm)	-0.005
Y$_{111}$(N/m^3)	1.848×10^{9}	χ_1 (C/m)	-0.013
λ_1(N/V^2)	3.27×10^{-5}	G_{11}(C/m^2)	-1.21×10^{3}
E_{1111}(kg/m^2)	1.001×10^{4}	L_{111}(C/m^3)	-120.144
F_{11}(N/mV)	-1.32×10^{3}	C_p(C/V)	1.915×10^{-8}
D_{111}(N/m^{2}V)	-117.54	c_{4v}(C/V^2)	5.335×10^{-7}
Δ_1(kg)	-9.343	$k_1 = \sigma_1$(C/mV)	1.217×10^{-4}

The experimental and numerical results of the output voltage are compared using the identified parameters in Figure 3.4. The experimental and numerical results are demonstrated to match well around the peak voltage. When nonlinear behaviour emerges at accelerations greater than 4 g, numerical results diverge from experimental ones, especially away from the peak frequencies. The eccentricity arises because the proposed models assume that the PVEH is being excited around its natural frequency. Furthermore, it is essential to design the PVEH being excited around the natural frequency to harvest the maximum available energy.

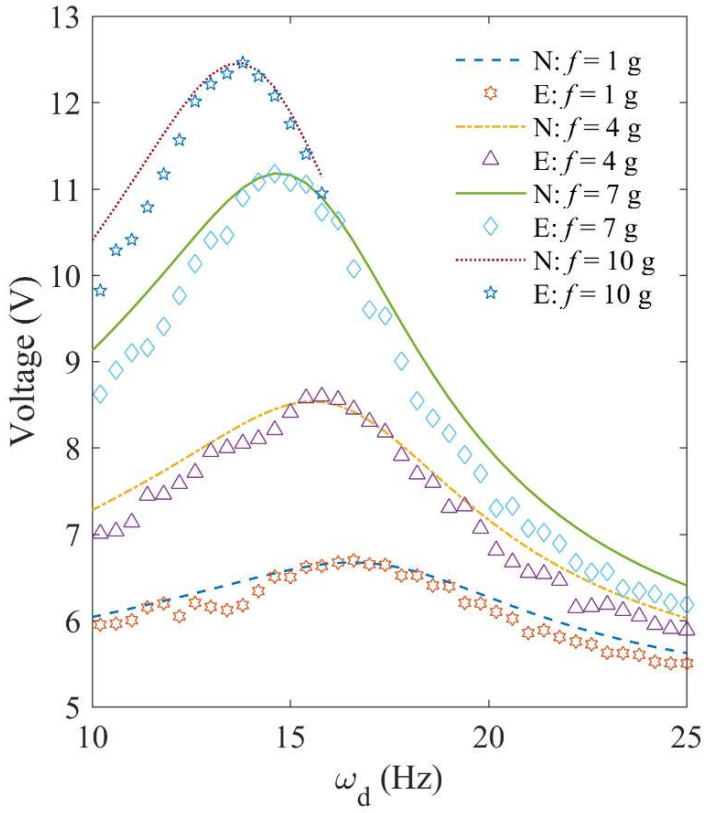

Figure 3.4 The experimental and numerical output voltage for acceleration amplitude of 1g, 4g, 7g, and 10g. (N: Numerical, E: Experimental)

In conclusion, the proposed formulae are capable of estimating the performance of the parabolic tapered PVEH. It's also been observed that raising the excitation

amplitude above 4 g causes softening effects, rendering the linear results invalid. As a result, when the excitation amplitude increases, designing the PVEH utilizing nonlinear formulae is necessary.

3.4 Effects of the Taper Parameter

In this part, the taper parameter's effect on the proposed parabolic tapered PVEH's nonlinear behaviour is investigated when the base excitation amplitude is increased from 1g to 10g. For this, a harvester with configuration parameters t_p = 0.254 mm, l_e = 72 mm, b_0 = 50 mm, t_h = 0.5 mm, M_{LM} = 15.1808 gram is considered along with four taper parameters as ϕ = 0 (uniform), 0.2, 0.4, and 0.6. Figure 3.5 shows the proposed PVEH's voltage curves for four different taper parameters and excitation amplitudes. For a detailed investigation of the taper parameter's effects, all the cases' backbone curves are plotted by joining the peaks of the voltage curves in the Figures. 3.5a - 3.5d and shown in Figure 3.6. The generated voltage decreased significantly with an increase in the taper parameter at higher excitation amplitudes, while the response is changed marginally at lower speeds. It can also be observed that, for the higher taper parameter values, the backbone curve is more bent than the lower ones (uniform width), which indicates a significant influence of the nonlinearities associated with higher taper parameters. Even though it is concluded that varying the width reduces the generated voltage from the PVEH, the harvested voltage-per-total mass (VPM) of the PVEH should be the performance assessment standard.

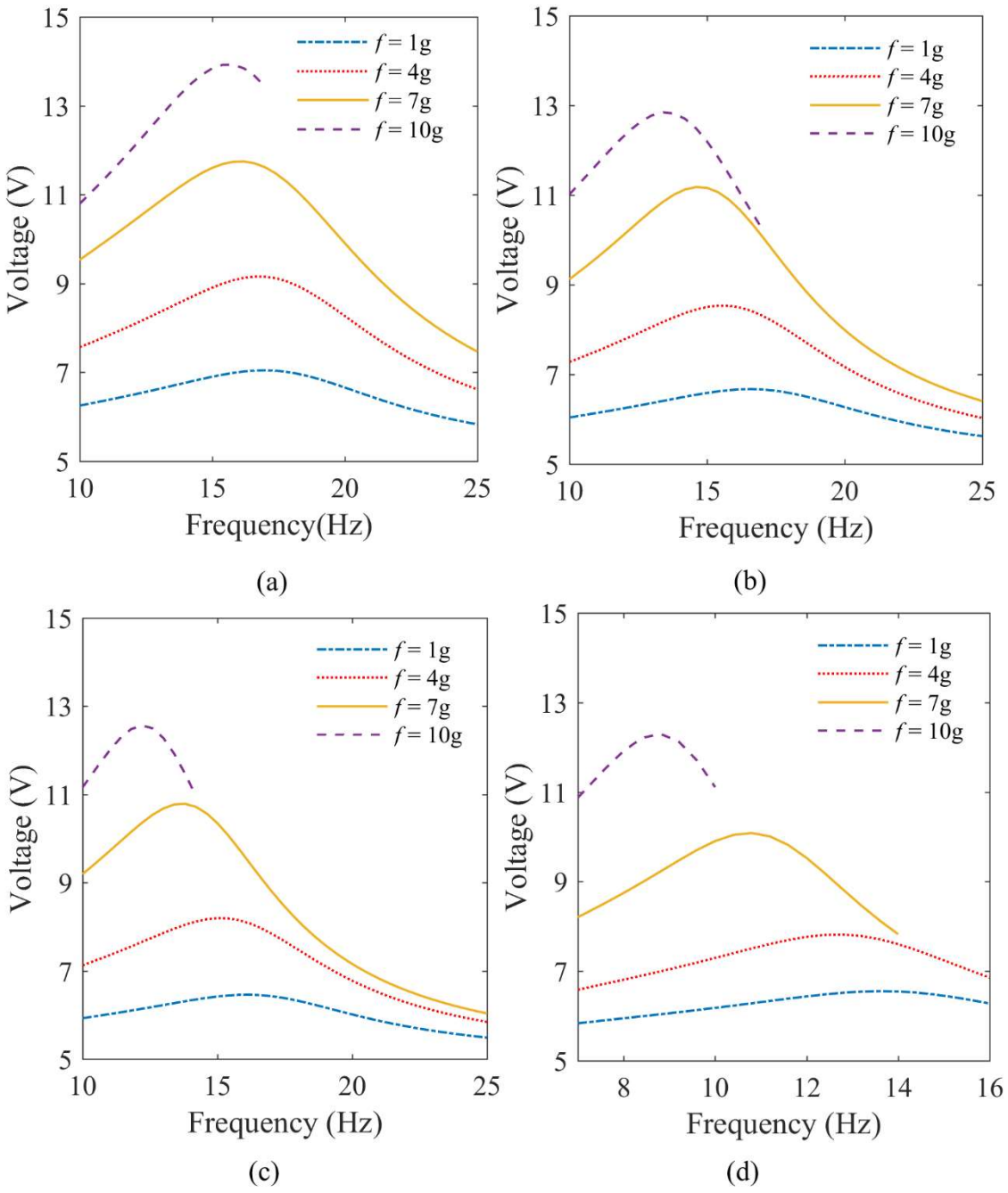

Figure 3.5 The generated output voltage from the PVEH models with taper parameters (a) $\phi = 0$, (b) $\phi = 0.2$, (c) $\phi = 0.4$, and (d) $\phi = 0.6$

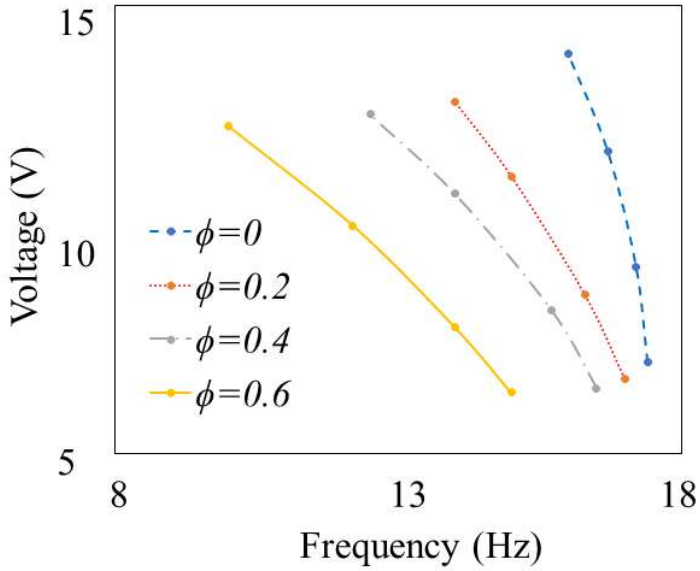

Figure 3.6 The output voltage backbone curves for the four different models (Figures 3.5a – 3.5d)

Additionally, the harvester's performance should be compared for the systems with identical natural frequencies because the vibration energy harvesters are always designed for operating at a definite excitation frequency. Therefore, all the considered models' principal natural frequencies are adjusted to attain the values equal to the uniform width harvester by altering the tip load mass value accordingly with the taper parameter variation. Figure 3.7 represents the models' backbone curves with identical first natural frequencies for the excitation amplitude variation from 1 g to 10 g. The harvester's behaviour is linear when the excitation amplitude is 1 g, and the highest VPM of the PVEH is observed at their respective natural frequencies. An increase in the excitation amplitude deviates the peak values from the natural frequencies of the presented models. Moreover, the VPM of the PVEH is not essentially reduced by varying the width as the mass and the voltage is decreased simultaneously. The VPM of the uniform coupled beam is the lowermost, which means that the power output from the PVEH is enhanced by tapering the width. Therefore, parabolic tapering cross-

sections is advantageous as it generates more power at a specific excitation amplitude and frequency. For the present model, the VPM of the harvester with $\phi = 0.6$ is 16.30% higher than the uniform width counterpart under 10g acceleration.

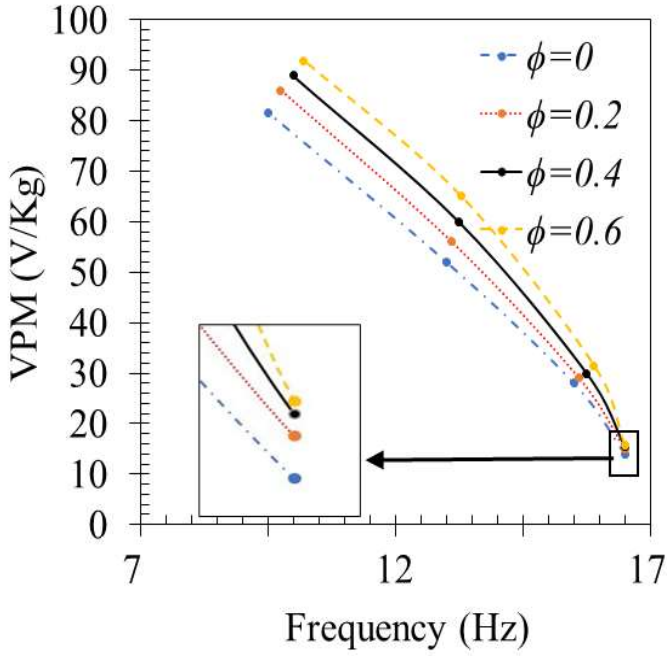

Figure 3.7 The output voltage backbone curves for the models with identical first natural frequencies

The comparison of the linear and nonlinear formulations is made by plotting the VPM of the harvester against the excitation amplitudes for different taper parameters and shown in Figure 3.8. The results' detailed analysis shows that the linear formulations are invalid for excitation amplitude higher than 2.5 g. Under this excitation, the eccentricity is 14.02% between the linear and nonlinear formulations. At higher excitation amplitudes, the eccentricity is very high. The system's performance under 7 g and 10 g excitation levels is given in Table 3.3 to compare the linear and nonlinear results. It is observed that the linear solutions are unsatisfactory for these high

excitation amplitudes, and the maximum difference is around 63.51%. Moreover, the harvester's VPM is also improved by increasing the taper parameter for every base excitation amplitude.

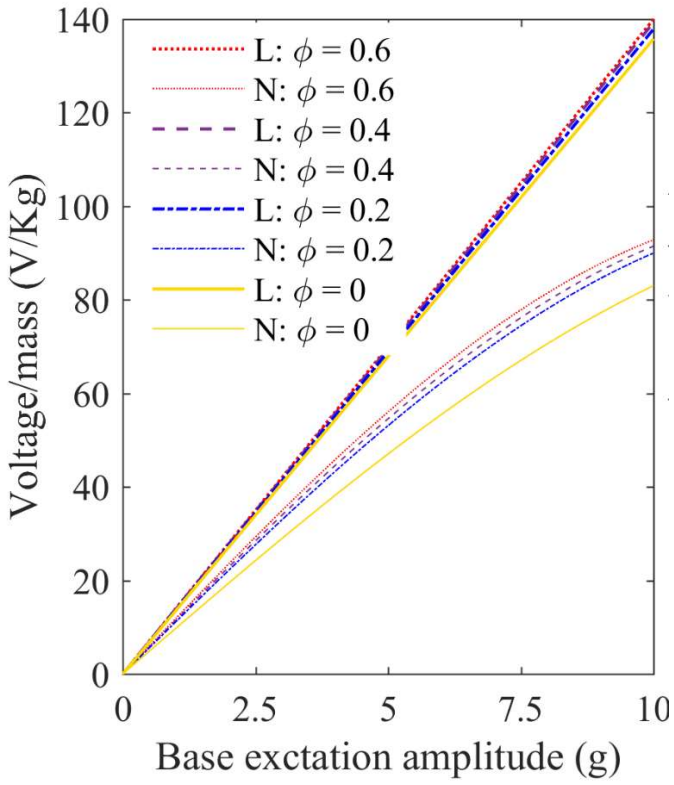

Figure 3.8 Comparison of the VPM using linear and nonlinear solutions for variation in taper parameters and excitation amplitudes

A more effective performance evaluating criteria of the PVEH is the PPM. Therefore, the harvester's PPM obtained using the linear and nonlinear models are shown in Figure 3.9. It can be noticed that the eccentricity between the linear and nonlinear solutions is more than 10% for excitations above 3.5 g. Therefore, the nonlinear formulation is more effective for estimating the PPM of the proposed harvester. Despite the VPM, the PPM of the harvesters from the nonlinear result is ordered equal to the linear counterpart, concluding that tapering the width decreases the PPM of the harvester for both linear and nonlinear formulations.

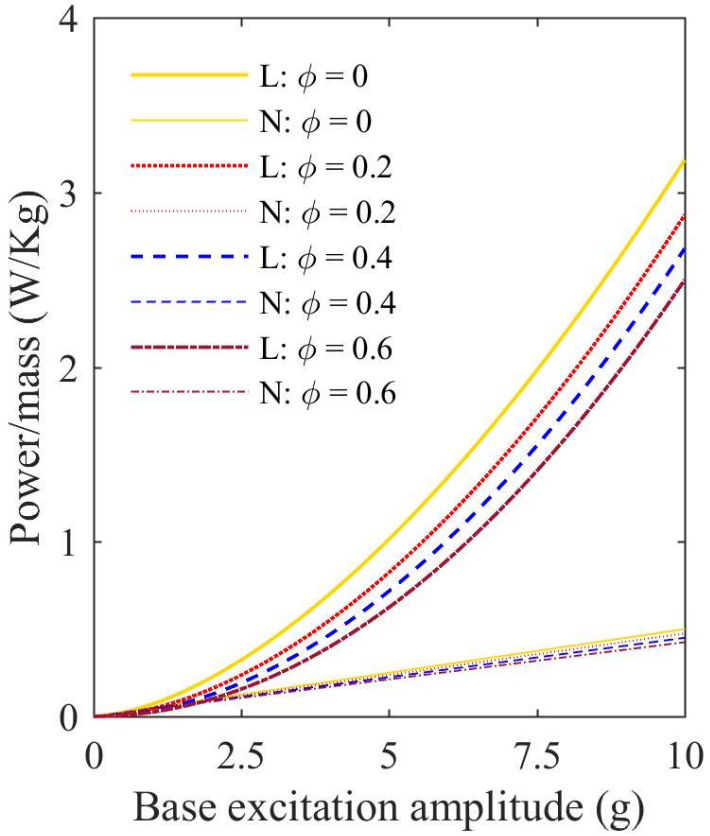

Figure 3.9 Comparison of the PPM calculated using linear and nonlinear solutions for variation in taper parameters and excitation amplitudes, across an optimum load resistance 300 kΩ

Table 3.4 Comparison of the linear and nonlinear VPM of the PVEH for 7 g and 10 g base excitation amplitudes

	Excitation amplitude (7g)				Excitation amplitude (10g)			
	$\phi = 0$	$\phi = 0.2$	$\phi = 0.4$	$\phi = 0.6$	$\phi = 0$	$\phi = 0.2$	$\phi = 0.4$	$\phi = 0.6$
NVPM(V/Kg)	63.34	70.61	75.62	79.34	83.05	90.01	94.08	96.59
LVPM(V/Kg)	95.06	96.53	97.51	98.00	135.8	137.9	139.3	140.1
Eccentricity (%)	50.07	36.71	28.94	23.51	63.51	53.20	48.06	44.94

3.5 Effects of the Piezoelectric Patch Thickness

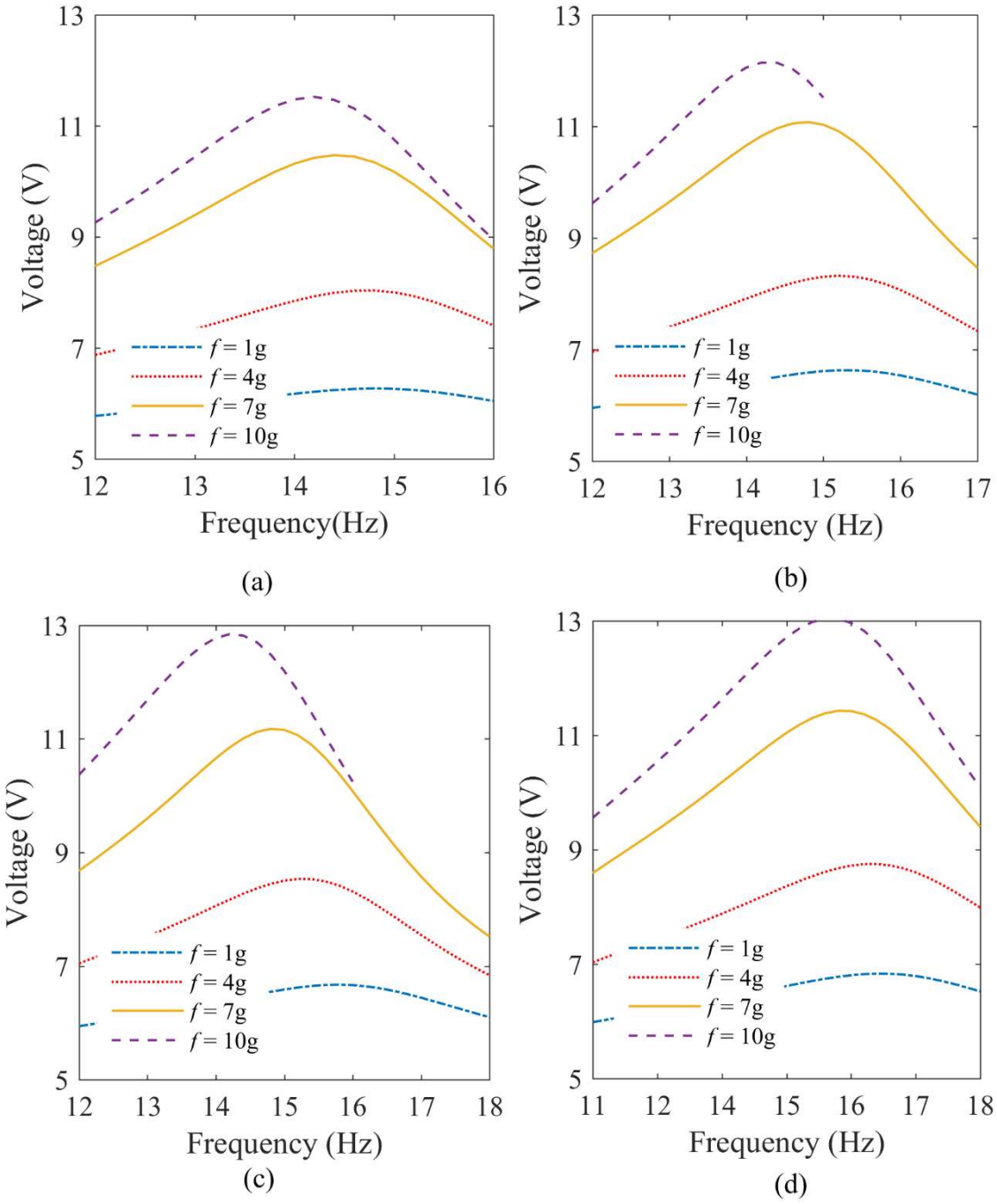

Figure 3.10 The output voltage from the PVEH models with $\phi = 0.2$ and piezoelectric patch thickness (a) $t_p = 0.15$ mm, (b) $t_p = 0.20$ mm, (c) $t_p = 0.25$ mm, and (d) $t_p = 0.30$ mm

In this part, the effect of the piezoelectric patch thickness on the proposed parabolic tapered PVEH's nonlinear behaviour is investigated when the base excitation is varied from 1 g to 10 g. For this, a harvester with configuration parameters ϕ = 0.2, l_e = 72 mm, b_0 = 50 mm, t_h = 0.5 mm, M_{LM} = 15.1808 gram is considered along with four values of the piezoelectric patch thickness as t_p = 0.15, 0.20, 0.25, and 0.30 mm. Figure 3.10 shows the proposed PVEH's voltage curves for four different piezoelectric patch thicknesses and excitation amplitudes.

For a detailed investigation of the piezoelectric patch thickness's effects, all the case's backbone curves are plotted by joining the peaks of the voltage curves in Figures 3.10a-3.10d and shown in Figure 3.11. It is observed that the nonlinearity and the generated voltage increase with an increase in the piezoelectric patch thicknesses. However, the system's natural frequency increases with an increase in the piezoelectric patch thickness, which puts a constraint on using thicker piezoelectric patches for vibration energy harvesting. Figure 3.12 presents the models' backbone curves with identical first natural frequencies for the excitation amplitude variation from 1g to 10g. The backbone curves are less responsive to the variation in piezoelectric patch thickness than the variation in the taper parameter. The maximum VPM of the PVEH is achieved for the thinnest piezoelectric patch (t_p = 0.15 mm). However, a diminished scope of harvesting the maximum available abundant vibration energy and the harvester's maximum transverse deflection puts a constraint on applying thinner piezoelectric patches for energy harvesting purposes.

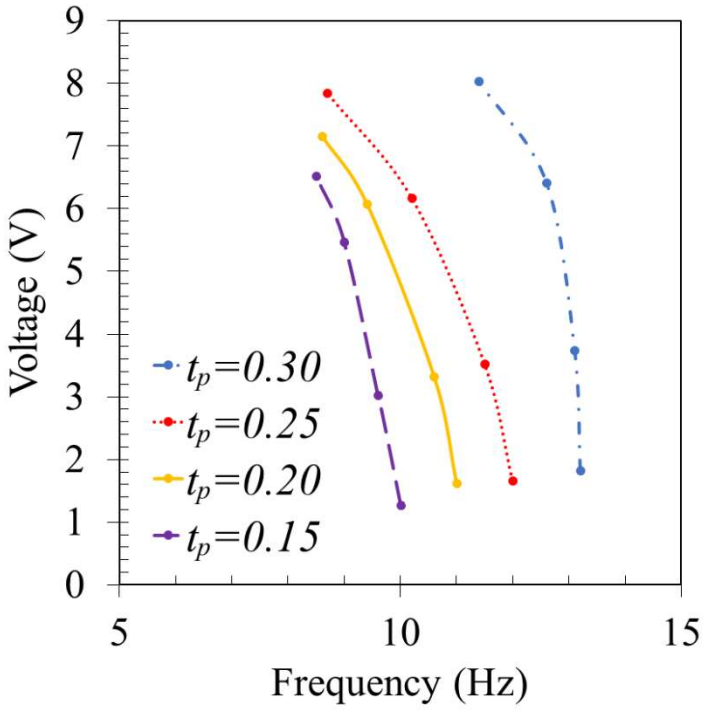

Figure 3.11 The output voltage backbone curves for the four different models (Figures 3.8a – 3.8d)

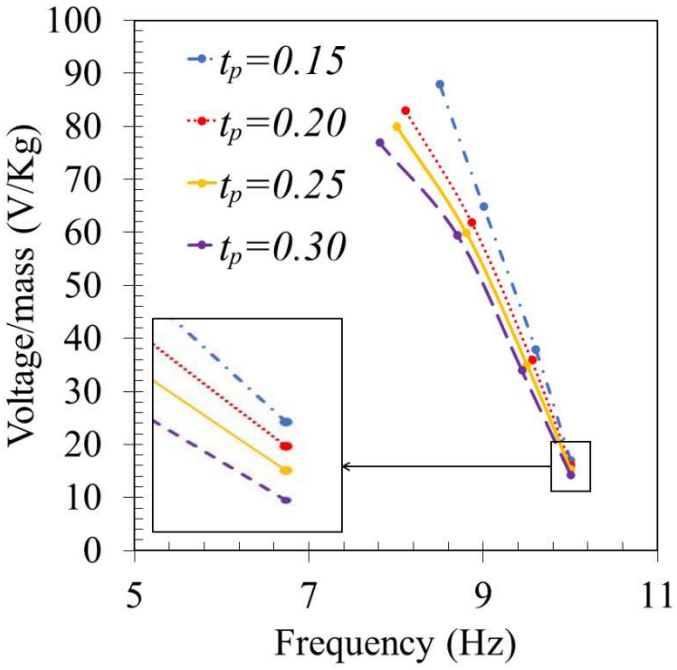

Figure 3.12 The output voltage backbone curves for the models with identical first natural frequencies

Therefore, the piezoelectric patch thickness should be chosen carefully so that the harvester can withstand a certain deflection to produce a high VPM while less contributing towards nonlinearity. For the present model, the VPM of the harvester with t_p = 0.15 mm is 10.24% higher than the model with t_p = 0.30 mm under 10 g acceleration.

The comparison of the linear and nonlinear formulations is made by plotting the VPM of the harvester against the excitation amplitudes for different piezoelectric patch thicknesses, shown in Figure 3.13a. The detailed analysis of the results shows that the linear formulations are invalid for excitation amplitude higher than 2.5 g. For this excitation, the eccentricity is 12.02% between the linear and nonlinear results, confirming that the linear formulation is inaccurate for calculating the PVEH's performance above 2.5 g excitation. At higher excitation amplitudes, the eccentricity is very high. The system's response for the exciting accelerations 4 g, 7 g, and 10 g is given in Table 3.5 to compare the linear and nonlinear results. It is observed that the linear solutions are unsatisfactory for these high excitation amplitudes, and the maximum difference is around 64.47% for 10 g acceleration and t_p = 0.30 mm. Moreover, the harvester's VPM also decreases with the increase in the piezoelectric patch thickness for every base excitation amplitude. The harvester's PPM for both linear and nonlinear models is given in Figure 13b. It can be observed that the thickening of the piezoelectric patch increases the peak output voltage but decreases the PPM of the harvester for both the linear and nonlinear systems.

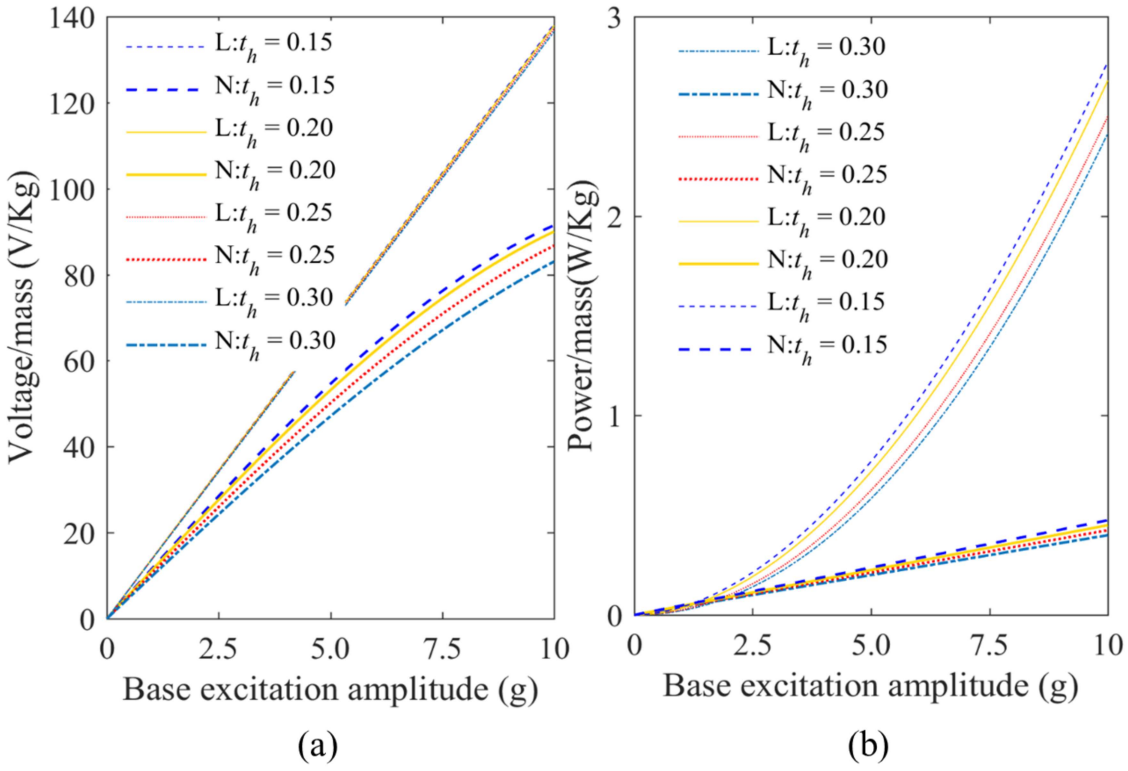

Figure 3.13 Comparison of the linear and nonlinear solutions for variation in the piezoelectric patch thickness and excitation amplitudes (a) VPM and (b) PPM, across an optimum load resistance 300 kΩ

Table 3.5 Comparison of the linear and nonlinear VPM of the PVEH for 4 g, 7 g, and 10 g base excitation amplitudes

	Excitation amp. (4 g)			Excitation amp. (7 g)			Excitation amp. (10 g)		
t_p (mm)	NVPM (V/Kg)	LVPM (V/Kg)	Ecc.* (%)	NVPM (V/Kg)	LVPM (V/Kg)	Ecc. (%)	NVPM (V/Kg)	LVPM (V/Kg)	Ecc. (%)
0.15	44.60	55.25	23.88	72.10	96.70	34.12	91.50	138.26	51.10
0.20	43.20	55.10	27.54	70.61	96.53	36.70	90.01	137.91	53.20
0.25	40.90	54.65	33.62	67.52	96.10	42.33	86.70	137.20	58.24
0.30	38.10	54.60	43.30	63.70	95.60	50.07	83.00	136.51	64.47

*Ecc.:- Eccentricity, amp.:- Amplitude

3.6 Summary

This chapter reports a full nonlinear formulation for a parabolic converging width unimorph PVEH with tip load mass under the influence of base excitation. The nonlinearities associated with the geometry and piezoelectric material are considered in the mathematical model. The mass normalized mode shapes are obtained using Galerkin's discretization technique. The solutions of the system are acquired with the help of the MMS and chain rule. The accuracy of the formulations is verified using experimental methods and comparing with other nonlinear formulations. Finally, the effects of the taper parameter and the piezoelectric patch thickness on the nonlinearity of the PVEH are studied.

Initially, the taper parameter and the piezoelectric patch thickness are varied while keeping the other system parameters constant. The output voltage curves are obtained for four different taper parameters and piezoelectric patch thicknesses under base excitation ranging from 1 g - 10 g. The results show that decreasing the harvesting beam's width and the piezoelectric patch's thickness decreases the PVEH's output voltage. After that, the tip load mass is changed in accordance with the taper parameter and the piezoelectric patch thickness to tune the natural frequencies of the considered models to match each other at a fixed value of frequency. The backbone plots for VPM against the base excitation amplitudes are obtained to analyze the tuned models' output performance. The results demonstrate that the tapered PVEH generates higher VPM than its uniform width counterpart. A similar trend is observed for VEH with a thinner piezoelectric patch. At 10 g acceleration, the VPM of the harvester with ϕ=0.6 is found to be 16.30% higher than the uniform width counterpart and the PVEH with t_p = 0.15

mm is 10.24% higher than the model with t_p =0.30 mm. The VPMs of the linear and nonlinear models are also analyzed, and it is observed that the linear formulations are not adequate for excitation amplitudes above 2.5 g. At higher excitation amplitudes, an extreme eccentricity is observed between the linear and nonlinear solutions. At 10 g acceleration, the maximum eccentricity of 64.47% and 63.51% is observed for the VEH model with $\phi = 0.2$, $t_p = 30$ mm, and $\phi = 0$, $t_p = 20$ mm, respectively.

To conclude, increasing the taper parameter and decreasing the piezoelectric patch thickness of the proposed parabolic tapering width piezoelectric PVEH may increase the output VPM. Even though the VPM of the harvester is enhanced, parabolic tapering the width of the harvesting structure may not increase the PPM for higher excitation levels. Reducing the piezoelectric patch thickness limits the maximum deflection that the harvesting beam can withstand and diminishes the scope of harvesting the maximum available abundant vibration energy. Therefore, the system configurations must be selected cautiously, and the nonlinear analysis is inevitable for high excitation amplitude applications.